

**Erbium-implanted materials for quantum communication applications**

Paul Stevenson <sup>1</sup>, Christopher M. Phenicie <sup>2</sup>, Isaiah Gray,<sup>2</sup> Sebastian P. Horvath,<sup>2</sup> Sacha Welinski,<sup>3</sup> Austin M. Ferrenti <sup>4</sup>, Alban Ferrier,<sup>5,6</sup> Philippe Goldner,<sup>5</sup> Sujit Das,<sup>7</sup> Ramamoorthy Ramesh,<sup>8,9,10</sup> Robert J. Cava,<sup>4</sup> Nathalie P. de Leon <sup>2</sup> and Jeff D. Thompson<sup>2,\*</sup>

<sup>1</sup>*Department of Physics, Northeastern University, Boston, Massachusetts 02115, USA*

<sup>2</sup>*Department of Electrical Engineering, Princeton University, Princeton, New Jersey 08544, USA*

<sup>3</sup>*Thales Research and Technology, 1 Avenue Augustin Fresnel, 91767 Palaiseau, France*

<sup>4</sup>*Department of Chemistry, Princeton University, Princeton, New Jersey 08544, USA*

<sup>5</sup>*Chimie ParisTech, PSL University, CNRS, Institut de Recherche de Chimie Paris, 75005 Paris, France*

<sup>6</sup>*Faculté des Sciences et Ingénierie, Sorbonne Université, UFR 933, 75005 Paris, France*

<sup>7</sup>*Materials Research Center, Indian Institute of Science, Bangalore 560012, India*

<sup>8</sup>*Department of Materials Science and Engineering, University of California, Berkeley, California 94720, USA*

<sup>9</sup>*Materials Sciences Division, Lawrence Berkeley National Laboratory, Berkeley, California 94720, USA*

<sup>10</sup>*Department of Physics, University of California, Berkeley, California 94720, USA*



(Received 14 October 2021; revised 21 March 2022; accepted 6 May 2022; published 10 June 2022)

Erbium-doped materials can serve as spin-photon interfaces with optical transitions in the telecom *C* band, making them an exciting class of materials for long-distance quantum communication. However, the spin and optical coherence times of  $\text{Er}^{3+}$  ions are limited by currently available host materials, motivating the development of new  $\text{Er}^{3+}$ -containing materials. Here we demonstrate the use of ion implantation to efficiently screen prospective host candidates, and show that disorder introduced by ion implantation can be mitigated through post-implantation thermal processing to achieve inhomogeneous linewidths comparable to bulk linewidths in as-grown samples. We present optical spectroscopy data for each host material, which allows us to determine the level structure of each site, allowing us to compare the environments of  $\text{Er}^{3+}$  introduced via implantation and via doping during growth. We demonstrate that implantation can generate a range of local environments for  $\text{Er}^{3+}$ , including those observed in bulk-doped materials, and that the populations of these sites can be controlled with thermal processing.

DOI: [10.1103/PhysRevB.105.224106](https://doi.org/10.1103/PhysRevB.105.224106)

**I. INTRODUCTION**

Quantum networks have a myriad of applications, including fundamentally secure communication [1], modular quantum computing [2], and precision measurement [3]. This has motivated substantial theoretical and experimental efforts to realize scalable schemes for both long-distance quantum communication and microwave-to-optical transduction. A major goal is to develop single atom quantum memories that can be deployed in quantum repeater architectures [4,5].

Experimentally realizing a robust quantum network—particularly one capable of operating over long distances—is a challenging prospect. The qubits at the heart of these systems must simultaneously satisfy several criteria: Long-lived quantum memories (often realized as electron or spin coherences), high rate of generation of indistinguishable photons (constraining excited state lifetime and spectral stability of the optical transition), and efficient initialization, manipulation, and detection schemes are the minimum requirements. However, there are several other factors which must be considered for real-world implementation: Wavelength (and attenuation

length in fibers or free space), inhomogeneous linewidth (which may allow frequency-selective multiplexing, or may require frequency tuning of individual defects), and the scalability of the material system.

Erbium-based systems are promising candidates for both single atom quantum memories in long-distance quantum networks and microwave-to-optical quantum state transduction. Many of the essential requirements for quantum networks have been demonstrated in  $\text{Er}^{3+}$ -containing systems, such as long electron [6] and nuclear [7] spin coherence times, telecom-wavelength spin-photon interfaces [8], and frequency-selective control of individual ions [9]. However, demonstrating the full range of properties required to realize a practical quantum network with  $\text{Er}^{3+}$  remains an outstanding challenge.

Many of the systems characterized for quantum information applications are yttrium-based crystals (e.g.,  $\text{Y}_2\text{SiO}_5$ ,  $\text{YVO}_4$ ).  $\text{Er}^{3+}$  readily substitutes for the  $\text{Y}^{3+}$  site, but the large spin bath formed by the  $^{89}\text{Y}$  nuclear spins has deleterious effects on spin and optical coherence times. While extremely long optical coherence times can be observed in  $\text{Er}^{3+}:\text{Y}_2\text{SiO}_5$  ( $T_2 = 4.38$  ms at 1.5 K and 7 T [10]), these optical coherence times are ultimately limited by the presence of  $^{89}\text{Y}$  nuclei [11], motivating the development of nuclear spin-free host

\*jthompson@princeton.edu

materials. Practically achieving a nuclear spin-free material will ultimately require isotopic enrichment; this requires stable spin-zero isotopes of each elemental component exist and the nuclear spin-full components are initially present in low levels.

However,  $\text{Er}^{3+}$  in non-yttrium materials has been studied in a variety of other contexts, such as infrared-to-visible up-conversion [12], laser gain media [13], and as probes of the local crystal environment [14], demonstrating that there is a rich chemical space still to explore for quantum information applications. Efficiently exploring this space and screening potential new materials remains an outstanding challenge [15].

A further challenge is encountered when integrating the current generation of  $\text{Er}^{3+}$ -containing materials with nanophotonic structures; while nanophotonic integration can enable single-ion detection [16] and quantum state transduction [17], the emitters addressed by the device are typically within hundreds of nanometers of the surface. Surface-related noise processes (trapped charges, dangling bonds, etc.) can substantially degrade the optical and spin coherence of nearby emitters [8,16,18]. Developing new material systems with reduced sensitivity to surface noise—either through nonpolar local symmetry, or fortuitously small Stark coefficients—may help enable stable, narrow optical transitions in these nanophotonic devices. These new materials would enable nanophotonic integration with implanted single crystal substrates as a “top-down” alternative to other cavity-emitter architectures such as nanoparticles in fiber cavities [19].

We recently demonstrated that  $\text{Er}^{3+}$  implanted in rutile  $\text{TiO}_2$  exhibits inhomogeneous optical linewidths below 500 MHz, among the narrowest inhomogeneous linewidths reported for any host material for  $\text{Er}^{3+}$  [20] and especially remarkable for ion-implanted  $\text{Er}^{3+}$ . Here we build on this result, using the same methodology to explore the properties of several other  $\text{Er}^{3+}$ -implanted materials. By utilizing ion implantation to introduce  $\text{Er}^{3+}$  into a variety of materials, we are able to rapidly generate and screen new material systems while also ensuring our results are representative of the properties of the near-surface ions required for nanophotonic integration.

The paper is structured as follows: In Sec. II we outline the criteria for host material selection; Sec. III briefly outlines the experimental methods; Secs. IV–VI present results for cubic, nonpolar, and polar symmetry crystals, respectively; and Sec. VII concludes with general observations.

## II. HOST MATERIAL CRITERIA

To narrow our search, we begin with a coarse set of criteria for prospective host crystals which can be determined from the elemental composition or from readily available reference data. Specifically, we search for material properties that allow for long  $\text{Er}^{3+}$  coherence times, and a material band gap sufficient to host the optical transition. An extensive tabulation of materials satisfying these properties was presented in Ref. [15].

Long spin coherence times require an environment with low magnetic noise. Thus, a good host material should be diamagnetic, composed of elements with nuclear spin-free isotopes, and have minimal paramagnetic impurities. Spin

coherence is ultimately limited by spin-lattice relaxation, but this can typically be suppressed by going to sufficiently low temperatures [22].

Coherent optical transitions are an essential element of a spin-photon interface. Optical coherence introduces two requirements; first, the band gap of the host material must be large enough such that emission from the defect optical transition is not reabsorbed by the host material ( $>0.83$  eV for  $\text{Er}^{3+}$ ), and second, the optical transition frequency should be stable in the presence of the solid state environment. One approach to realizing this second requirement is to optimize crystal growth and processing to remove sources of noise [23], while a complimentary strategy is to minimize the sensitivity of the qubit to these noise sources. If the symmetry of the crystal site does not allow a permanent electric dipole moment, then the Stark shift from electric field noise is quadratic instead of linear. Narrow ( $<500$  MHz) inhomogeneous linewidths previously reported in  $\text{Er}$ -implanted  $\text{TiO}_2$  were attributed to the nonpolar symmetry (and thus vanishing first-order Stark shift) of the  $\text{Er}^{3+}$  site in this material [20], and inversion-symmetric group IV-vacancy defects in diamond have significantly less spectral diffusion near surfaces and in nanostructures [24,25] compared to NV centers [23].

Below, we present the optical characterization of a selection of  $\text{Er}$ -implanted materials which meet the criteria outlined earlier: They are composed of elements which have stable nuclear spin-free isotopes, band gaps greater than 1 eV, and which span a wide range of potential coordination environments for implanted  $\text{Er}^{3+}$ . By probing both the inhomogeneous linewidths and implantation yield for particular sites we are able to gain insight into both the static disorder in the crystal and the sensitivity of  $\text{Er}^{3+}$  to noise sources in the crystal. These crystals span a wide range of potential  $\text{Er}^{3+}$  coordination environments: Cubic ( $\text{MgO}$ ,  $\text{PbTiO}_3$ ,  $\text{SrTiO}_3$ ,  $\text{ZnS}$ ), noncubic and nonpolar ( $\text{TiO}_2$ ,  $\text{PbWO}_4$ ), and polar symmetries ( $\text{MoO}_3$ ,  $\text{ZnO}$ ).

This wide-ranging screening approach allows us to identify  $\text{MgO}$ ,  $\text{PbWO}_4$ ,  $\text{TiO}_2$ , and  $\text{ZnO}$  as particularly promising candidates, each showing narrow inhomogeneous linewidths for near-surface ions. In several material systems we also demonstrate the importance of post-implantation thermal processing.

## III. EXPERIMENTAL APPROACH

$\text{Er}^{3+}$  is incorporated into host materials via ion implantation (Innovion) at energies up to 350 keV, which corresponds to an implantation depth of  $\approx 100$  nm in the materials studied here (see [26] for full implantation recipe). The implantation process creates a highly nonequilibrium distribution of  $\text{Er}^{3+}$  coordination environments and implantation-induced vacancies. To identify different  $\text{Er}^{3+}$  environments in the host crystals and characterize their properties, we employ photoluminescence-excitation (PLE) spectroscopy, described below. These techniques enable us to ascertain the site-specific level structure of different  $\text{Er}^{3+}$  environments and their associated inhomogeneous linewidths. In many cases we observe only lower-lying  $Z$  and  $Y$  states, which is discussed in the Supplemental Material (SM) [26]. Samples are mounted in a sample-in-vapor optical cryostat held at 4.5 K unless otherwise noted. Multiple samples are mounted on the same copper

cold finger with GE varnish, using copper barriers between samples to prevent scattered light from exciting fluorescence in adjacent samples.

An achromatic doublet lens outside the cryostat is used to focus excitation light and collect emission from the sample, and a tunable narrowband laser (CTL 1500, Toptica) is used to excite the sample. The resulting emission passes through a polarizing beam splitter to filter residual scattered excitation light, and the emission is detected using either an amplified photodiode (Femto systems OE-200-IN2) or a grating spectrometer with a cooled InGaAs detector array (PyLON-IR, Teledyne Princeton Instruments), enabling us to generate two-dimensional maps of the emission spectrum for various excitation wavelengths. Fast thermalization of the  $\text{Er}^{3+}$  excited states (relative to the millisecond radiative lifetime [27]) results in identical emission spectra for each  $\text{Er}^{3+}$  site regardless of which transition was excited; thus when  $\text{Er}^{3+}$  can occupy multiple different sites the emission spectrum can be used to group excitation peaks originating from  $\text{Er}^{3+}$  ions occupying the same site.

With site-specific excitation and emission frequencies, we can extract the ground and excited state energies for each site. The ground state splits into eight states  $Z_1$ – $Z_8$ , (five in cubic symmetry), while the excited state splits into seven states  $Y_1$ – $Y_7$  (five in cubic symmetry). For each site we also measure the excited state lifetime, which we can compare to the expected magnetic dipole (MD) decay rate [28]. This allows us to estimate the role of forced electric dipole moments in the decay rate, which are only allowed in sites without inversion symmetry.

## IV. CUBIC SYSTEMS

### A. MgO

*Structure and properties:* MgO adopts the cubic halite structure, with octahedrally coordinated (local  $O_h$  symmetry)  $\text{Mg}^{2+}$  and  $\text{O}^{2-}$ . The only native nuclear spin present at an appreciable level is  $^{25}\text{Mg}$  ( $I = \frac{5}{2}$ , 10% natural abundance).

MgO has a relatively low refractive index ( $n = 1.71$ ) [29], which is advantageous for improving refractive index contrast in hybrid nanophotonic devices. The large band gap of MgO (7.8 eV) is sufficient to host not only telecom-wavelength optical transitions, but can also host defects with shorter wavelength transitions.

The samples used in this work had a (001) surface and were purchased from MTI Corp. Samples were stored in a desiccator when not in use because of the hygroscopic nature of MgO. Prior to implantation, no  $\text{Er}^{3+}$  emission was observed.

*Optical spectrum:* The excitation-emission spectrum of MgO shown in Fig. 1 has a rich structure with peaks corresponding to at least five distinct incorporation sites. We focus our discussion on the most intense set of peaks, highlighted with blue arrows in Fig. 1 (other energy levels are tabulated in the SM [26]). The lowest two excitation peaks show small splittings (0.08 and 0.3  $\text{cm}^{-1}$ , respectively) which are suggestive of some degeneracy-lifting perturbation. Substantial unresolved fine structure is evident in the  $Z_1 \rightarrow Y_1$  peak (Fig. 2), making quantitative determination of inhomogeneous linewidth challenging; however, we can put an upper bound

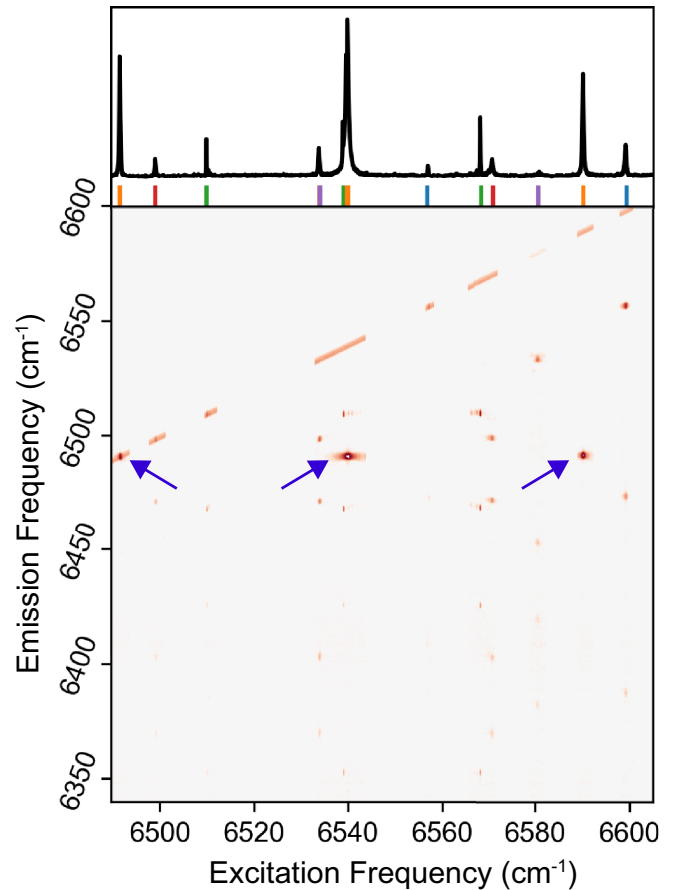


FIG. 1. Top panel: Excitation spectrum of annealed  $\text{Er}^{3+}:\text{MgO}$  at  $T = 4.5$  K, showing all transitions observed. Colored bars indicate different sites. Bottom panel: Excitation-emission spectrum of the same sample, plotted on a log intensity axis to show all peaks observed. The diagonal feature at  $\omega_{\text{exc}} = \omega_{\text{em}}$  is from scattered excitation light, and provides a wavelength reference for the spectrometer.

of 2 GHz on the width of each peak (post-thermal processing), comparable to the inhomogeneous linewidth observed in many yttrium-based crystals [27].

The fluorescence lifetime of the  $Y_1$  level is 20.1 ms (see the SM [26]). We can estimate the expected radiative lifetime of a magnetic dipole (MD) transition by scaling the lifetime in the free  $\text{Er}^{3+}$  ion (98.3 ms) by  $n^3$  (to account for the higher density of states in the crystal), which yields an estimated MD lifetime of 19.6 ms [28]. The good agreement with the experimental value suggests that there is no forced electric dipole contribution and that nonradiative relaxation pathways are not significant in this case.

Previous ESR measurements have reported that  $\text{Er}^{3+}$  occupies the octahedral  $\text{Mg}^{2+}$  substitutional site [14,21], and has a quartet ground state ( $\Gamma_8$  in the Koster notation), rather than the usual Kramers doublet. Strain can lift this fourfold degeneracy [14], consistent with the closely spaced sets of peaks observed in our measurements. Using previously reported crystal field parameters [21,30], we determine that the transition from  $Y_1$  to the lowest nonquartet state ( $\Gamma_7 \rightarrow \Gamma_6$ ) is symmetry forbidden. To determine the ground-state splittings, we increase the

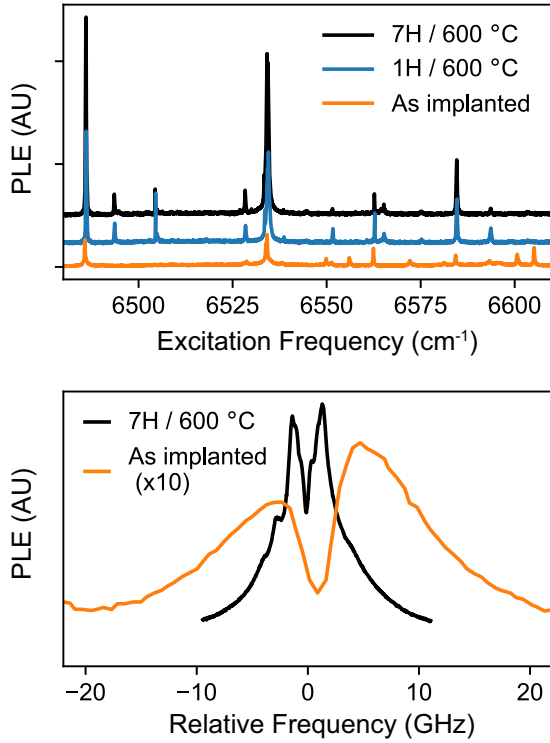


FIG. 2. Upper panel: Changes in the number and intensities of peaks in MgO as a function of annealing conditions, described in the main text. Bottom panel: High-resolution scan of the  $Z_1 \rightarrow Y_1$  transition, showing the change in linewidth on annealing.

temperature of the sample to populate the  $Y_2$  level. Emission from this level allows us to determine the ground-state splittings, which are in excellent agreement with previously reported models based on ESR measurements for the substitutional  $Mg^{2+}$  site (Table I) [21].

*Annealing:*  $Er^{3+}$ -implanted MgO was annealed in air for a total of 7 h at 600 °C. Previous studies of MgO implanted with Fe have indicated aggregation and precipitation above this temperature [31]. Post-anneal spectra show a sevenfold increase in the intensity of the  $O_h$  site. We also observe a number of peaks after annealing which we suggest may be associated with structural configurations where charge compensation occurs locally (as in  $Nd^{3+}$  in  $CaF_2$  [32]), though

the detailed structure and symmetry of this site are unknown. (The level structure for this site is detailed in [26]). A number of small peaks initially present in the as-implanted sample disappear on annealing. Figure 2 shows the dependence of the peak intensities on annealing conditions.

The increase in intensity of the site 1 peaks with annealing indicates that thermal processing is important for  $Er^{3+}$ -implanted MgO, though the results here likely do not represent the optimal annealing method. The detailed mechanism and optimization of this thermal processing will be the focus of future work.

## B. $PbTiO_3 : SrTiO_3$

*Structure and properties:*  $PbTiO_3$  and  $SrTiO_3$  are both perovskite structures, with cuboctahedral coordination of the A site ( $Pb^{2+}$ ,  $Sr^{2+}$ ) and octahedral coordination of the B site ( $Ti^{4+}$ ). Below 105 K,  $SrTiO_3$  undergoes a symmetry-lowering tetragonal distortion [33], lowering the local symmetry of the A and B sites to  $D_{2d}$  and  $C_{4h}$ , respectively [34]. Both Ti and Pb have isotopes with nuclear spin,  $^{207}Pb$  ( $I = \frac{1}{2}$ , 22% natural abundance),  $^{47}Ti$  ( $I = \frac{5}{2}$ , 7% natural abundance), and  $^{49}Ti$  ( $I = \frac{7}{2}$ , 5% natural abundance).

This sample is not implanted with  $Er^{3+}$ ; doping is instead introduced during growth of the  $PbTiO_3$  layer. 100 nm of  $PbTiO_3$  is overgrown on a  $SrTiO_3$  substrate via pulsed-laser deposition, as detailed in the SM [26]. The  $Er^{3+}$  doping is modulated such that only one unit-cell layer is doped with  $Er^{3+}$  at 0.1 mol%, then ten layers are undoped, then another unit-cell layer is doped, and so on. Thin-film and layered structures present an alternative approach to integrating quantum emitters with nanophotonic structures; they avoid the generation of vacancies and other damage centers during implantation, but can be challenging systems to realize ultralow doping in a controlled manner. Both  $SrTiO_3$  and  $PbTiO_3$  have high refractive indices ( $n = 2.28$  [35] and  $n < 2.5$  [36], respectively).

*Optical spectrum:* In contrast to MgO,  $Er^{3+} : PbTiO_3 : SrTiO_3$  shows a much simpler spectrum, shown in Fig. 3. All peaks show the same emission pattern, consistent with a single occupied site. The extracted crystal field levels are given in Table I.

TABLE I. Crystal field energies and other properties of cubic-symmetry host materials. Lifetimes predicted for purely magnetic-dipole transitions are given in parentheses. Crystal field levels for the Y levels are given relative to the  $Z_1 \rightarrow Y_1$  transition energy. Levels assigned to strain-split quartet states are given in the same table entry. States which are not observed in our experiments are denoted with asterisks.

	MgO			$PbTiO_3 : SrTiO_3$		ZnS			
	Experiment		Cubic model [21]	Experiment		Site 1		Site 2	
$Z_1 \rightarrow Y_1$ $cm^{-1}$	6491.5		N/A	6511.7		6489.3		6486.7	
$n$ (energies in $cm^{-1}$ )	$Z_n$	$Y_n$	$Z_n$	$Z_n$	$Y_n$	$Z_n$	$Y_n$	$Z_n$	$Y_n$
1	0.0, 0.08	0.0	0.0, 0.0	0.0	0.0	0.0	0.0	0.0	0.0
2	110.4	48.3, 48.6	111.2	14.21	73.7	7.4	6.7	11.2	5.7
3	134.8	98.7	139.7	113.47	75.1	25.6	30.7	31.4	16.7
4	*	*	619.2	*	204.8	*	39.6	*	49.0
Lifetime/ms	20.1 (19.6)		N/A	3.9 (6.3)		4.6 (8.4)		5.6 (8.4)	

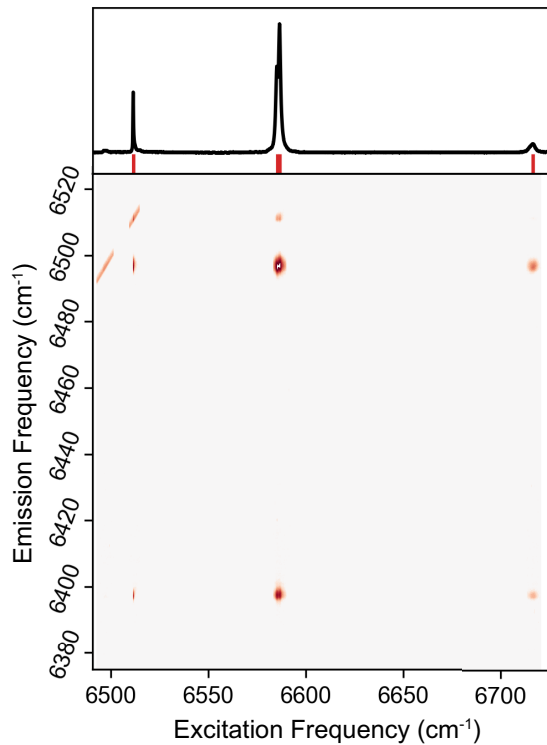


FIG. 3. Top panel: Excitation spectrum of  $\text{Er}^{3+}$ -doped  $\text{PbTiO}_3$ :  $\text{SrTiO}_3$ , showing all transitions observed. Bottom panel: Excitation-emission spectrum of the same sample, plotted on a log intensity axis to show all peaks observed.

The inhomogeneous linewidth of the  $Z_1 \rightarrow Y_1$  transition is  $\approx 9$  GHz, with an asymmetric tail. The excited state lifetime of the  $Y_1$  state is 3.9 ms. The expected magnetic dipole radiative lifetime is 6.3 ms, which is indicative of a forced electric dipole contribution to the emission.

While our measurements do not allow us to unambiguously assign a site to the incorporated  $\text{Er}^{3+}$ , we note that ESR measurements of  $\text{Er}^{3+}$  in  $\text{BaTiO}_3$  have suggested  $\text{Er}^{3+}$  can substitute in either the A or B site [37], and the better matching of ionic radius between  $\text{Er}^{3+}$  and  $\text{Pb}^{2+}$  with respect to  $\text{Ba}^{2+}$  suggests A-site (distorted cubeoctahedral) substitution might be expected. The A site ( $D_{2d}$  symmetry at low temperature) permits an electric dipole contribution to the radiative lifetime via  $d-f$  mixing, while the B-site symmetry ( $C_{4h}$ ) does not.

### C. ZnS

*Structure and properties:* ZnS adopts the zinc blende structure, composed of tetrahedrally coordinated  $\text{Zn}^{2+}$  and  $\text{S}^{2-}$ . Only the  $^{67}\text{Zn}$  isotope has nonzero spin ( $I = \frac{5}{2}$ , natural abundance 4%). ZnS has a refractive index  $n = 2.27$  [38] and a band gap of 3.5 eV.

The samples described in this work were purchased from SurfaceNet, with (111) orientation, grown by a seeded vapor-phase free growth method. No  $\text{Er}^{3+}$  emission was observed prior to implantation.

*Optical spectrum:* Two distinct sites (sites 1 and 2) can be identified in the ZnS excitation-emission spectrum, shown in Fig. 4. We note that for both sites, the transitions span a much

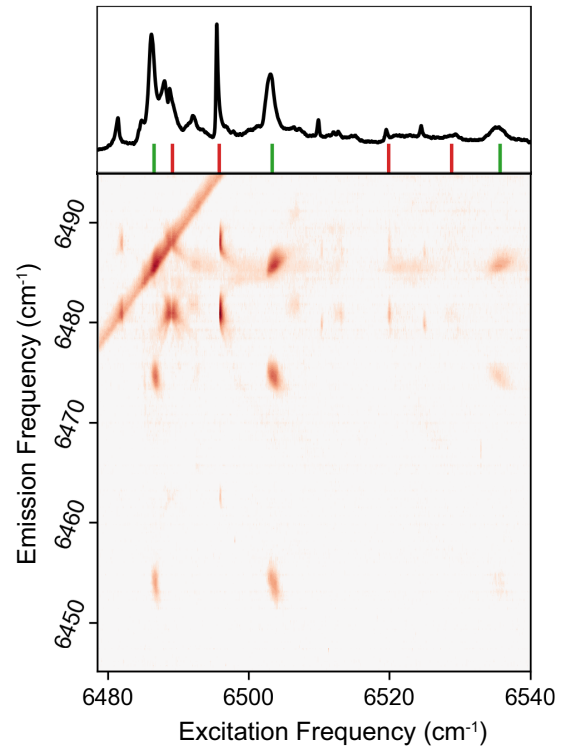


FIG. 4. Top panel: Excitation spectrum of  $\text{Er}^{3+}$ -implanted ZnS (annealed), showing all transitions observed. Bottom panel: Excitation-emission spectrum of the same sample, plotted on a log intensity axis to show all peaks observed.

smaller energy range than either MgO or  $\text{PbTiO}_3$ :  $\text{SrTiO}_3$ . Extracted crystal field levels are reported in Table I.

The measured excited state lifetimes for both sites 1 (4.6 ms) and 2 (5.6 ms) are shorter than expected for a pure MD transition (8.4 ms). The congested spectrum makes accurate determination of the inhomogeneous linewidths difficult, even with site-selective measurements, but both sites 1 and 2 have  $Z_1 \rightarrow Y_1$  inhomogeneous linewidths of  $>25$  GHz.

Emission in the visible wavelength range from  $\text{Er}^{3+}$ -implanted ZnS has been previously reported using cathodoluminescence [39], where two sites were also observed. The Z levels we determine for site 2 are in excellent agreement with the reported levels for the substitutional  $\text{Zn}^{2+}$  site. Moreover, the population of this site increased with annealing in a manner consistent with previous reports [39].

However, the parameters we determine for site 1 are not consistent with the reported levels for the interstitial site identified in Ref. [39] despite similar implantation fluences and subsequent annealing. One possible explanation for this discrepancy is the excitation method; cathodoluminescence, and resonant excitation may excite sites with different efficiencies. Though we do not propose a detailed structural assignment for site 1, we note that some charge compensation must occur in ZnS with  $\text{Er}^{3+}$  defects (as with all the materials we present here); differences in charge compensation (e.g., local or remote, compensating ion identity, local configuration) would be expected to give rise to distinct sites.

*Annealing:*  $\text{Er}^{3+}$ -implanted ZnS was annealed in air at  $350^\circ\text{C}$  for 3 h, as described in Ref. [39]. Prior to annealing,

TABLE II. Crystal field energies and other properties of nonpolar symmetry host materials. Lifetimes predicted for purely magnetic-dipole transitions are given in parentheses. Crystal field levels for the  $Y$  levels are given relative to the  $Z_1 \rightarrow Y_1$  transition energy.

$Z_1 \rightarrow Y_1/\text{cm}^{-1}$	PbWO <sub>4</sub>		TiO <sub>2</sub>	
	6517.7		6575.7	
$n$ (energies in $\text{cm}^{-1}$ )	$Z_n$	$Y_n$	$Z_n$	$Y_n$
1	0.0	0.0	0.0	0.0
2	10.7	3.6	35.0	14.8
3	31.9	47.6	40.8	22.9
4	51.4	103.4	119.6	96.3
5	189.5	134.9	169.7	*
6	228.7	147.6	208.3	*
7	253.3	165.4	269.8	*
8	282.1	N/A	*	N/A
Lifetime/ms	7.7 (>9.1)		5.25 (5.2–6) [20]	

site 1 was observable, but no clear emission from site 2 was detected. After annealing, emission from site 2 increased substantially, having similar maximum peak height to site 1.

## V. NONCUBIC, NONPOLAR SYSTEMS

### A. PbWO<sub>4</sub>

*Structure and properties:* PbWO<sub>4</sub> adopts the Scheelite crystal structure, in which the optical properties of doped rare-earth ions have been extensively studied [40]. Both Pb and W have isotopes with nuclear spin <sup>207</sup>Pb ( $I = \frac{1}{2}$ , 22% natural abundance) and <sup>183</sup>W ( $I = \frac{5}{2}$ , 14% natural abundance). We observe Er<sup>3+</sup> emission in our PbWO<sub>4</sub> prior to implantation, suggesting low levels of native doping; this would suggest that extra care may be required during synthesis to minimize additional paramagnetic defects. Similar background levels of Er<sup>3+</sup> have been observed in other nominally lanthanide-free materials [41].

PbWO<sub>4</sub>, like all Scheelite structures, is birefringent. The refractive indices at 1530 nm are  $n_o < 2.21$  and  $n_e < 2.16$  (estimated from [42]). Numerous values have been reported for the band gap of PbWO<sub>4</sub>, but all are  $>3.5$  eV. CaWO<sub>4</sub>, which we compare PbWO<sub>4</sub> with below, has the same structure and similar optical properties ( $n_o = 1.88$ ,  $n_e = 1.9$  [35], band gap 4.2 eV). In Er<sup>3+</sup>-doped CaWO<sub>4</sub>, Er<sup>3+</sup> is known to occupy the Ca<sup>2+</sup> site, which has local  $S_4$  symmetry [40,43].

The PbWO<sub>4</sub> substrate with (001) orientation was purchased from MTI Corp. The comparison CaWO<sub>4</sub> sample was grown via the Czochralski method, with Er<sup>3+</sup> doping of approximately 0.8 ppb [44].

*Optical spectrum:* We compare the optical properties of three samples: Er<sup>3+</sup>-implanted PbWO<sub>4</sub>, PbWO<sub>4</sub> with native Er<sup>3+</sup> (presumably introduced during crystal growth), and as a reference sample, Er<sup>3+</sup>-doped CaWO<sub>4</sub>. By comparing the intensities of the observed spectra in the implanted and unimplanted PbWO<sub>4</sub>, we estimate the background Er<sup>3+</sup> doping levels to be on the  $<$  ppb level.

The excitation-emission spectrum of implanted PbWO<sub>4</sub> (Fig. 5) shows only one site. The peaks are all clearly resolvable, allowing the determination of all eight  $Z$  levels and all seven  $Y$  levels (Table II). The splittings reported are

qualitatively similar to those known for isostructural Er<sup>3+</sup>-doped CaWO<sub>4</sub> [40].

The excited state lifetime of implanted PbWO<sub>4</sub> is 7.7 ms, shorter than the 9.3 ms expected from a pure MD transition, suggesting a forced electric dipole contribution. The  $Z_1 \rightarrow Y_1$  transition of the implanted sample (Fig. 6) shows significant structure, but the FWHM of the central peak is approximately 1 GHz. As noted earlier, our PbWO<sub>4</sub> samples have trace Er<sup>3+</sup> contamination pre-implantation, enabling us to directly compare implanted and bulk Er<sup>3+</sup> in PbWO<sub>4</sub> (Fig. 6). We find that the peak positions are identical between the implanted

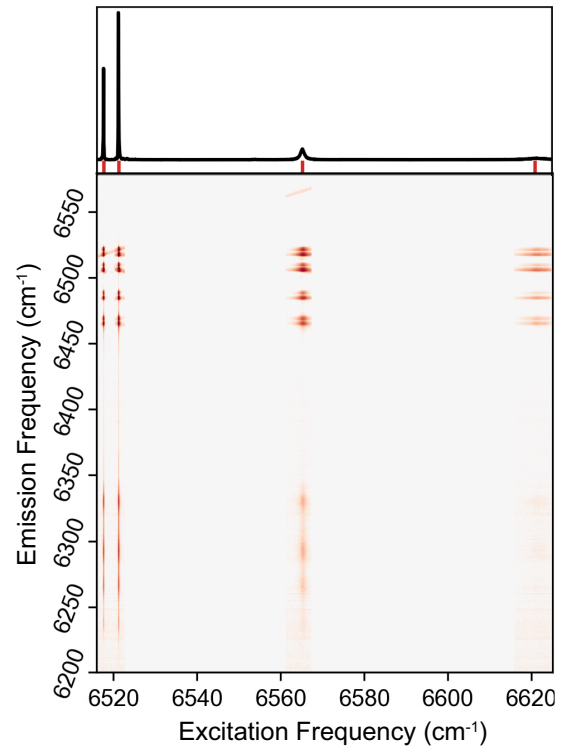


FIG. 5. Top panel: Excitation spectrum of Er<sup>3+</sup>-implanted PbWO<sub>4</sub> (annealed). Bottom panel: Excitation-emission spectrum of the same sample, plotted on a log intensity axis to show all peaks observed.

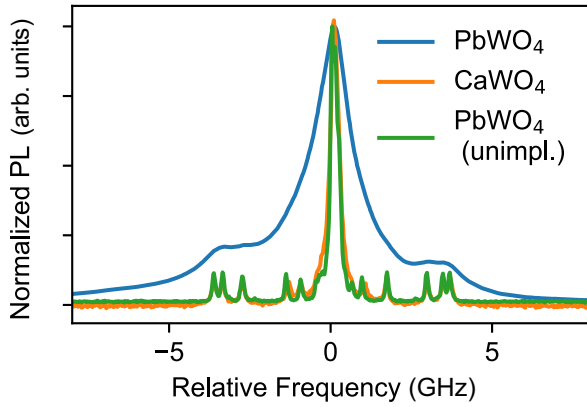


FIG. 6. High resolution scan of  $Z_1 \rightarrow Y_1$  transition for implanted  $\text{PbWO}_4$ , bulk-doped  $\text{CaWO}_4$ , and unimplanted  $\text{PbWO}_4$  with trace  $\text{Er}^{3+}$  impurities. The same hyperfine structure is observed in all cases.  $\text{PbWO}_4$  and  $\text{CaWO}_4$  spectra are shifted by their respective  $Z_1 \rightarrow Y_1$  transition energies, but the frequency axis is not otherwise altered.

and trace- $\text{Er}^{3+}$  samples, though the bulk  $\text{Er}^{3+}$  inhomogeneous linewidths are threefold narrower. This might suggest there is still some residual disorder from implantation; however, we also note that our local  $\text{Er}^{3+}$  concentration is high ( $\approx 100$  ppm) in the implanted region, and 1 GHz inhomogeneous linewidths have been observed in bulk-doped  $\text{Er}^{3+}$ :  $\text{CaWO}_4$  of similar concentrations [13].

To further explore the similarities between  $\text{CaWO}_4$  and  $\text{PbWO}_4$ , we compare the spectrum of the implanted  $\text{PbWO}_4$  and a bulk-doped  $\text{CaWO}_4$  sample. The same hyperfine structure around the  $Z_1 \rightarrow Y_1$  transitions is observed for both  $\text{CaWO}_4$  and  $\text{PbWO}_4$ , which arises from the 23% natural abundance  $^{167}\text{Er}$ . The near perfect correspondence between the  $\text{PbWO}_4$  and  $\text{CaWO}_4$  spectra suggest their hyperfine constants (and thus underlying  $g$  tensors) are extremely similar, from which we conclude that  $\text{Er}^{3+}$  occupies a similar site in both cases. In  $\text{CaWO}_4$ ,  $\text{Er}^{3+}$  is known to occupy the substitutional cation site [40,43].

The prominent hyperfine-split transitions are a result of the large transverse component of the hyperfine tensor [40]; this acts in the same manner as a large off-axis magnetic field, giving rise to optical transitions which flip the electron or nuclear spin. Well-resolved hyperfine transitions may find use in optical manipulation of the nuclear spin [45], potentially serving as an ancilla qubit.

*Annealing:* Implanted  $\text{PbWO}_4$  was annealed for 1 h at  $900^\circ\text{C}$ . Prior to annealing, the signal observed (both magnitude and linewidth) was similar to the native  $\text{Er}^{3+}$  in the unimplanted crystal, suggesting implanted  $\text{Er}^{3+}$  is not optically active. After annealing the sample the signal increased by a factor of  $>200$ .

## B. $\text{TiO}_2$

*Structure and properties:*  $\text{TiO}_2$  adopts the rutile structure in our samples. Previous studies of Er-implanted  $\text{TiO}_2$  demonstrated that the  $\text{Er}^{3+}$  occupies the substitutional Ti site, with local  $D_{2h}$  symmetry [20].

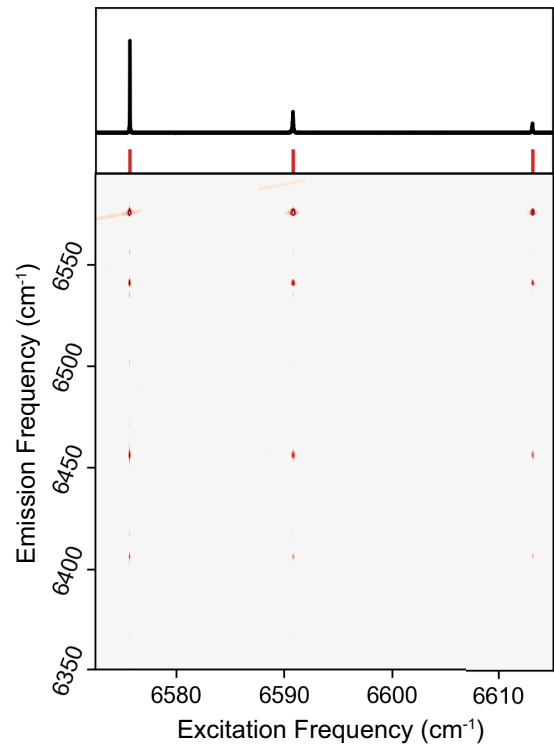


FIG. 7. Top panel: Excitation spectrum of  $\text{Er}^{3+}$ -implanted  $\text{TiO}_2$  (annealed), showing all transitions observed. Bottom panel: Excitation-emission spectrum of the same sample, plotted on a log intensity axis to show all peaks observed.

Ti has two isotopes with nuclear spin,  $^{47}\text{Ti}$  ( $I = \frac{5}{2}$ , 7% natural abundance) and  $^{49}\text{Ti}$  ( $I = \frac{7}{2}$ , 5% natural abundance).  $\text{TiO}_2$  has a large refractive index ( $n > 2.4$ ) and is highly birefringent. The band gap of  $\text{TiO}_2$  is 3.0 eV. The preparation of the samples described below have been previously described [20].

*Optical spectrum:* The excitation spectrum and inhomogeneous linewidth of implanted  $\text{TiO}_2$  have been previously reported in Ref. [20]. Here an improved optical setup enables us to report a more complete excitation-emission spectrum (Fig. 7), which is consistent with the previously reported crystal field levels (Table II). Experimental improvements in resolution and sensitivity allow us to report here several previously-unreported  $Z$  levels.

## VI. POLAR SYSTEMS

### A. $\text{MoO}_3$

*Structure:*  $\text{MoO}_3$  forms orthorhombic crystals composed of distorted octahedra of  $\text{Mo}^{6+}$  coordinated by  $\text{O}^{2-}$ . Only two sites of nontrivial symmetry are found in this crystal,  $C_s$  (Mo and O positions) and  $C_i$  (interstitial sites). Mo has two isotopes with nuclear spin,  $^{95}\text{Mo}$  ( $I = \frac{5}{2}$ , 15% natural abundance) and  $^{97}\text{Mo}$  ( $I = \frac{5}{2}$ , 10% natural abundance). The refractive index of  $\text{MoO}_3$  is  $n = 2.07$  [46]. The band gap of  $\text{MoO}_3$  is 3.2 eV [47]. The samples used in the work below were grown by the vapor transport method.

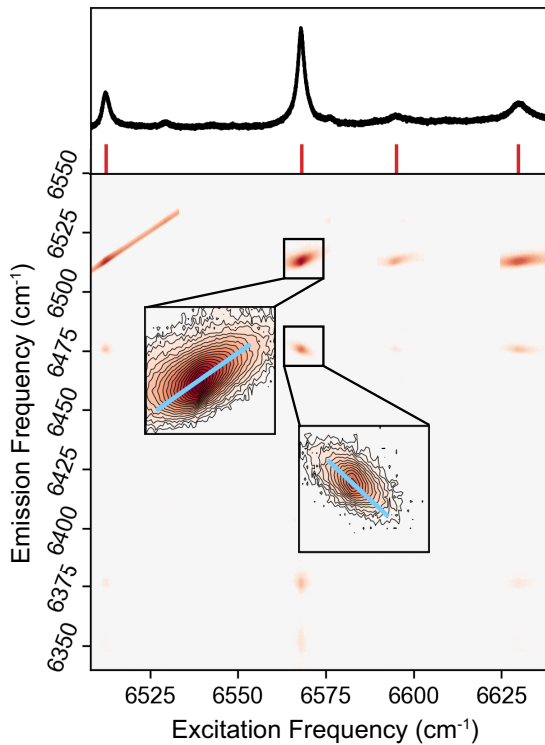


FIG. 8. Top panel: Excitation spectrum of Er<sup>3+</sup>-implanted MoO<sub>3</sub> (annealed), showing all transitions observed. Bottom panel: Excitation-emission spectrum of the same sample, plotted on a log intensity axis to show all peaks observed. Inset shows the correlated line shape in the excitation-emission spectrum for two peaks.

*Optical spectrum:* The spectrum of implanted MoO<sub>3</sub> is consistent with a single dominant environment for Er<sup>3+</sup>, showing a sparse pattern of excitation and emission peaks. The excited state lifetime of MoO<sub>3</sub> is 5.5 ms, shorter than the 11.0 ms expected from a pure magnetic dipole transition in this material. The inhomogeneous linewidth of the  $Z_1 \rightarrow Y_1$  transition is 90 GHz, which is the broadest linewidth we report here. There are several possible sources of disorder in this system; not only is Er<sup>3+</sup> in MoO<sub>3</sub> sensitive to implantation-induced damage, but the variety of oxidation states that can be adopted by Mo has the potential to serve as an intrinsic source of inhomogeneity.

The broad inhomogeneous linewidths in this sample highlight another source of information accessible from our spectroscopic approach. Several of the two-dimensional line shapes show distinct slopes (such as the inset of Fig. 8) which reveal the correlations between excitation and emission frequencies of subensembles of Er<sup>3+</sup> ions (e.g., a subensemble may have a redshifted  $Z_1 \rightarrow Y_1$  transition, but a blueshifted  $Z_1 \rightarrow Y_2$  transition). These correlations describe how the different energy levels of the Er<sup>3+</sup> ions shift in response to the main source of disorder in the system (electric field, strain, etc.), which may be useful in site assignment or identifying transitions which are minimally sensitive to the local disorder. This approach is currently limited by our spectrometer resolution ( $\approx 1$  cm<sup>-1</sup>), but improvements in detection resolution would allow this information to be extracted for narrower

inhomogeneous linewidths. Identified crystal field levels are listed in Table III.

*Annealing:* The implanted MoO<sub>3</sub> sample was annealed in air at 550 °C for 4 h. Previous studies assessing Er<sup>3+</sup>-implanted MoO<sub>3</sub> as a potential optoelectronic material found this annealing procedure increased the visible emission from Er<sup>3+</sup> in MoO<sub>3</sub> [48]. Er<sup>3+</sup> emission was observed both pre- and post-anneal, the main effect of the annealing was the removal of a number of small, barely resolvable peaks, but did not impact the inhomogeneous linewidth. Because of the irregular size and shape of the crystals, it is not possible to make a quantitative comparison between pre- and post-anneal peak heights. The post-anneal excitation-emission spectrum is consistent with a single environment for the implanted Er.

## B. ZnO

*Structure:* ZnO adopts the hexagonal Wurtzite structure. The Zn<sup>2+</sup> ion is coordinated by four O<sup>2-</sup> in a distorted tetrahedral fashion with C<sub>3v</sub> symmetry. The polar crystal structure of ZnO gives rise to a piezoelectric effect in the crystal. Only the <sup>67</sup>Zn isotope has nonzero spin ( $I = \frac{5}{2}$ , natural abundance 4%).

The refractive index of ZnO is  $n = 1.93$  [35], and the band gap is 3.3 eV. The samples described here had a (0001) orientation and were purchased from MTI Corp. No emission from Er<sup>3+</sup> was observed prior to implantation.

*Optical spectrum:* The optical spectrum of Er-implanted ZnO, shown in Fig. 9, is dominated by a single site. The inhomogeneous linewidth of the  $Z_1 \rightarrow Y_1$  transition is 1.5 GHz, which is among the narrowest of the materials we present here. This narrow linewidth is observed despite the polar symmetry and piezoelectric nature of the crystal. An interesting point of comparison here are “pseudo-C<sub>3v</sub>” defects in SiC, where similarity between dipoles in the ground and excited states results in minimal sensitivity of the optical transition to electric fields [49]. Identified crystal field levels are listed in Table III.

The lifetime of Er<sup>3+</sup>-ZnO is substantially smaller than would be expected for a magnetic-dipole transition (5.8 vs 13.6 ms), which indicates a forced electric dipole contribution.

Rutherford backscattering measurements of implanted ZnO have observed that Er<sup>3+</sup> occupies the substitutional Zn<sup>2+</sup> site [50], while optical measurements of Er<sup>3+</sup>-implanted GaN [51], which adopts the same structure and has similar lattice constants, also find that Er<sup>3+</sup> occupies the cation substitutional site. Our observation of a single, well-defined site in the excitation-emission spectrum is consistent with a picture of Er<sup>3+</sup> substituting for Zn<sup>2+</sup>, where the sparseness of the spectrum suggests either remote charge compensation or one dominant charge compensation configuration.

*Annealing:* ZnO was annealed at 750 °C for a total of 16 h; this was the total time at 750 °C over three annealing runs of duration 1, 6, and 9 h. Annealing at higher temperatures is known to lead to out-diffusion of Er<sup>3+</sup> [50]. As-implanted, the spectrum showed a wide range of low-intensity, spectrally broad features; after annealing for 1 h a new set of peaks with much narrower inhomogeneous linewidths was observed. The intensity of these peaks increased with longer annealing times, reaching a maximum increase of 10× relative to the

TABLE III. Crystal field energies and other properties of polar symmetry host materials. Lifetimes predicted for purely magnetic-dipole transitions are given in parentheses. Crystal field levels for the  $Y$  levels are given relative to the  $Z_1 \rightarrow Y_1$  transition energy.

$Z_1 \rightarrow Y_1 / \text{cm}^{-1}$	MoO <sub>3</sub>		ZnO	
	6512.5		6504.2	
$n$ (energies in $\text{cm}^{-1}$ )	$Z_n$	$Y_n$	$Z_n$	$Y_n$
1	0.0	0.0	0.0	0.0
2	36.5	55.6	19.8	14.8
3	135.6	82.5	27.8	22.9
4	163.0	117.2	116.9	*
5	177.4	*	152.9	*
6	*	*	195.4	*
7	*	*	217.8	*
Lifetime/ms	5.5 (11.0)		5.8 (13.6)	

as-implanted peak height. Spectra for these annealing steps are shown in the SM [26].

## VII. DISCUSSION

Ion implantation and doping during growth are two distinct approaches to introducing  $\text{Er}^{3+}$  ions into a host material; understanding to what extent the two approaches can generate similar coordination environments of  $\text{Er}^{3+}$  is necessary for exploring new host materials for quantum communication

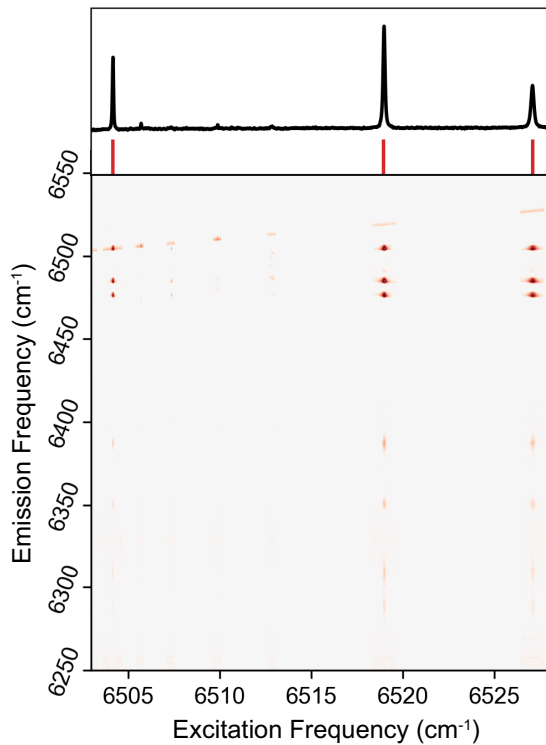


FIG. 9. Top panel: Excitation spectrum of  $\text{Er}^{3+}$ -implanted ZnO (annealed), showing all transitions observed. Bottom panel: Excitation-emission spectrum of the same sample, plotted on a log intensity axis. Several smaller features are visible in the excitation range 6507 to 6512  $\text{cm}^{-1}$ ; these are transitions from thermally populated states of the  $\text{Er}^{3+}$ .

applications. We find that, where the coordination environment for the doped samples is known (i.e.,  $\text{MgO}$ ,  $\text{PbWO}_4$ , and  $\text{ZnO}$ ), ion implantation is capable of generating the same local environment.

However, we are also able to identify several other sites occupied by implanted  $\text{Er}^{3+}$  in various samples using ion implantation. In  $\text{MgO}$  we can resolve at least four other sites in addition to the  $O_h$  site (detailed in the SM); multiple sites are observable in  $\text{ZnS}$ ; and the spectrum of  $\text{ZnO}$  does not resolve into a clear single site until the sample has been annealed. To explain this observation, we consider the effects of charge compensation and implantation-induced damage to the host crystal. In all systems described here,  $\text{Er}^{3+}$  is an aliovalent defect, requiring charge compensation in the crystal; different configurations of local charge compensation can give rise to multiple spectrally distinct peaks, as in the case of  $\text{Nd}^{3+}$  in  $\text{CaF}_2$  [32] and  $\text{Er}^{3+}$ : Si [52,53]. Additionally, ion implantation generates vacancy defects which may produce additional coordination environments of  $\text{Er}^{3+}$  which would not be observed in a sample doped during growth.

The effect of ion implantation damage is not limited to generating new, distinct,  $\text{Er}^{3+}$  sites, but can also give rise to disorder in the crystal host. The inhomogeneous linewidth reflects the extent of the disorder, as well as the sensitivity of the  $\text{Er}^{3+}$  optical transitions to this disorder. In multiple implanted systems ( $\text{MgO}$ ,  $\text{PbWO}_4$ ,  $\text{TiO}_2$ ,  $\text{ZnO}$ ) we see inhomogeneous linewidths on the order of a few GHz (summarized in Table IV), comparable to what is typically observed in conventional host materials such as  $\text{Er}^{3+}$ :  $\text{Y}_2\text{SiO}_5$  [27],

TABLE IV. Summary of the observed inhomogeneous linewidths for  $Z_1 \rightarrow Y_1$  transitions after thermal annealing.

Material	Inhomogeneous linewidth
$\text{MgO}$	<2 GHz
$\text{PbTiO}_3$ : $\text{SrTiO}_3$	9 GHz
$\text{ZnS}$	>25 GHz
$\text{PbWO}_4$	1 GHz
$\text{TiO}_2$	500 MHz
$\text{MoO}_3$	90 GHz
$\text{ZnO}$	1.5 GHz

TABLE V. Summary of the effects of annealing on different host materials.

Material	Effect of annealing	
	Site Occupancy	Inhomogeneous linewidth
MgO	$O_h$ site increases, additional sites also appear	Narrows, quartet splitting decreases
ZnS	Site 2 appears	No change
PbWO <sub>4</sub>	No implanted Er <sup>3+</sup> observable prior to annealing; large increase after anneal	N/A
TiO <sub>2</sub>	Increase in $D_{2d}$ site	Narrows
MoO <sub>3</sub>	Minor peaks disappear on annealing	No change
ZnO	Initial site disappears, replaced by new site	New site has tenfold narrower inhomogeneous linewidth

suggesting that the effect of static disorder in the implanted samples can be similar to that in doped materials. These linewidths will also include contributions from defects already present in the crystal, and may have scope for further improvement using optimized substrates. The presence of native Er<sup>3+</sup> ions in our unimplanted PbWO<sub>4</sub> samples enables a direct comparison of inhomogeneous linewidths between doped and implanted samples; here we observe that the implanted sample is approximately three times broader than the doped Er<sup>3+</sup>, but with a linewidth sufficiently narrow to resolve several hyperfine-related features.

A necessary tool in realizing these GHz-wide inhomogeneous linewidths, however, is thermal processing. The annealing conditions for each sample are given in the appropriate material section, but the effects we observe can be generally categorized as changing site occupancies and changing inhomogeneous linewidths. These effects are summarized in Table V. The effect of annealing is particularly striking in PbWO<sub>4</sub> and ZnO; in these cases, annealing significantly changes the nature of the implanted Er<sup>3+</sup> ions, which are not initially optically active in the case of PbWO<sub>4</sub> and occupy a highly disordered site in the case of ZnO. The thermal processing conditions we outline for each material do not necessarily represent the optimal conditions; given the complex interplay of Er<sup>3+</sup> diffusion, charge compensation, and implantation damage repair there is likely scope for improvement for each of the materials outlined here.

## VIII. OUTLOOK AND CONCLUSIONS

Several materials presented here are promising candidates for future single-Er<sup>3+</sup> studies. MgO is a low refractive index material with reports of millisecond spin  $T_1$  for Er<sup>3+</sup> at temperatures  $>1$  K [21], while PbWO<sub>4</sub> and CaWO<sub>4</sub> have interesting hyperfine structure which may be useful for initializing ancilla qubits. Our results enable us to identify a number of candidate systems which could support highly coherent optical transitions; specifically, the narrow inhomogeneous linewidths we observe in MgO, TiO<sub>2</sub>, PbWO<sub>4</sub>, and ZnO, suggest either the damage from implantation is minimal, or the  $Z_1 \rightarrow Y_1$  transition is insensitive to it. In either case, this suggests it may be possible to realize optical coherence times in these materials which are not degraded by ion implantation.

Beyond simply replacing yttrium-based crystals as passive host materials, both PbTiO<sub>3</sub> : SrTiO<sub>3</sub> and ZnO (which are respectively ferroelectric and piezoelectric) have promising optical properties. The prospect of long optical and spin coherence in polar crystals is particularly intriguing; the ability

to actively control the host material could enable rapid frequency tuning of optical transitions, novel control schemes [54,55], and spectral shaping of emitted photons [56].

The next step in developing these materials as potential components of a quantum network is to characterize their coherence properties (both optical and spin) through time-resolved approaches such as photon echo and spin echo measurements. These coherence times are important metrics for quantum networking applications; further exploring how the material properties, linewidths, and thermal processing we present here correlate with these coherence times will form the basis of future research. We also note that the implanted materials systems we present could be probed at both the single-ion and ensemble level, enabling the discrepancies between single-ion and bulk properties to be further explored [16].

While our discussion has focused on integration with nanophotonic devices, many of these materials may be useful in ensemble applications. Our results show that ion implantation can be used to identify promising candidate materials, which could then be doped during crystal growth. This would provide a route to combining the flexibility and relative ease of sample preparation associated with ion implantation with the higher doping levels and high-quality materials possible with careful crystal growth. More generally, the combination of ion implantation and thermal processing we present will enable efficient searches through material parameter space, providing new data which could be used in future computational or data-mining studies to identify new candidate hosts [15]. This approach is not limited to screening host materials, but could also be used to efficiently search for new emitters in established host materials [57–59].

## ACKNOWLEDGMENTS

Funding for this research was provided by the AFOSR (Contract No. FA9550-18-1-0334), the Eric and Wendy Schmidt Transformative Technology Fund at Princeton University, and the Princeton Catalysis Initiative. The materials processing work was supported by the U.S. Department of Energy, Office of Science, National Quantum Information Science Research Centers, Co-design Center for Quantum Advantage (C2QA) under Contract No. DE-SC0012704. P.G. acknowledges funding from ANR Mirespin project, Grant ANR-19-CE47-0011 of the French Agence Nationale de la Recherche. The work at UC Berkeley was supported by the Center for Probabilistic Spin Logic for Low-Energy Boolean

and Non-Boolean Computing (CAPSL), one of the Nano-electronic Computing Research (nCORE) Centers as task

2759.002, and a Semiconductor Research Corporation (SRC) program sponsored by the NSF through CCF 1739635.

- [1] A. K. Ekert, *Phys. Rev. Lett.* **67**, 661 (1991).
- [2] S. Wehner, D. Elkouss, and R. Hanson, *Science* **362**, eaam9288 (2018).
- [3] P. Kómár, E. M. Kessler, M. Bishof, L. Jiang, A. S. Sørensen, J. Ye, and M. D. Lukin, *Nat. Phys.* **10**, 582 (2014).
- [4] H. J. Kimble, *Nature (London)* **453**, 1023 (2008).
- [5] M. Atatüre, D. Englund, N. Vamivakas, S.-Y. Lee, and J. Wrachtrup, *Nat. Rev. Mater.* **3**, 38 (2018).
- [6] M. Le Dantec, M. Rančić, S. Lin, E. Billaud, V. Ranjan, D. Flanigan, S. Bertaina, T. Chanelière, P. Goldner, A. Erb, R. B. Liu, D. Estève, D. Vion, E. Flurin, and P. Bertet, *Sci. Adv.* **7**, eabj9786 (2021).
- [7] M. Rančić, M. P. Hedges, R. L. Ahlefeldt, and M. J. Sellars, *Nat. Phys.* **14**, 50 (2018).
- [8] M. Raha, S. Chen, C. M. Phenicie, S. Ourari, A. M. Dibos, and J. D. Thompson, *Nat. Commun.* **11**, 1605 (2020).
- [9] S. Chen, M. Raha, C. M. Phenicie, S. Ourari, and J. D. Thompson, *Science* **370**, 592 (2020).
- [10] T. Böttger, C. W. Thiel, R. L. Cone, and Y. Sun, *Phys. Rev. B* **79**, 115104 (2009).
- [11] T. Böttger, C. W. Thiel, Y. Sun, and R. L. Cone, *Phys. Rev. B* **73**, 075101 (2006).
- [12] B. Goleosorkhi, H. Nozary, A. Fürstenberg, and C. Piguet, *Mater. Horizons* **7**, 1279 (2020).
- [13] Y. Sun, C. Thiel, R. Cone, R. Equall, and R. Hutcheson, *J. Lumin.* **98**, 281 (2002).
- [14] J. M. Baker and G. Currell, *J. Phys. C* **9**, 3819 (1976).
- [15] A. M. Ferrenti, N. P. de Leon, J. D. Thompson, and R. J. Cava, *npj Comput. Mater.* **6**, 126 (2020).
- [16] A. M. Dibos, M. Raha, C. M. Phenicie, and J. D. Thompson, *Phys. Rev. Lett.* **120**, 243601 (2018).
- [17] J. G. Bartholomew, J. Rochman, T. Xie, J. M. Kindem, A. Ruskuc, I. Craiciu, M. Lei, and A. Faraon, *Nat. Commun.* **11**, 3266 (2020).
- [18] S. Sangtawesin, B. L. Dwyer, S. Srinivasan, J. J. Allred, L. V. H. Rodgers, K. De Greve, A. Stacey, N. Dontschuk, K. M. O'Donnell, D. Hu, D. A. Evans, C. Jaye, D. A. Fischer, M. L. Markham, D. J. Twitchen, H. Park, M. D. Lukin, and N. P. de Leon, *Phys. Rev. X* **9**, 031052 (2019).
- [19] B. Casabone, C. Deshmukh, S. Liu, D. Serrano, A. Ferrier, T. Hümmer, P. Goldner, D. Hunger, and H. de Riedmatten, *Nat. Commun.* **12**, 3570 (2021).
- [20] C. M. Phenicie, P. Stevenson, S. Welinski, B. C. Rose, A. T. Asfaw, R. J. Cava, S. A. Lyon, N. P. de Leon, and J. D. Thompson, *Nano Lett.* **19**, 8928 (2019).
- [21] M. Borg, R. Buisson, and C. Jacolin, *Phys. Rev. B* **1**, 1917 (1970).
- [22] R. Orbach, *Proc. R. Soc. London Ser. A* **264**, 458 (1961).
- [23] Y. Chu, N. de Leon, B. Shields, B. Hausmann, R. Evans, E. Togan, M. J. Burek, M. Markham, A. Stacey, A. Zibrov, A. Yacoby, D. Twitchen, M. Loncar, H. Park, P. Maletinsky, and M. Lukin, *Nano Lett.* **14**, 1982 (2014).
- [24] A. Sipahigil, K. D. Jahnke, L. J. Rogers, T. Teraji, J. Isoya, A. S. Zibrov, F. Jelezko, and M. D. Lukin, *Phys. Rev. Lett.* **113**, 113602 (2014).
- [25] B. C. Rose, D. Huang, Z.-H. Zhang, P. Stevenson, A. M. Tyryshkin, S. Sangtawesin, S. Srinivasan, L. Loudin, M. L. Markham, A. M. Edmonds, D. J. Twitchen, S. A. Lyon, and N. P. de Leon, *Science* **361**, 60 (2018).
- [26] See Supplemental Material at <http://link.aps.org/supplemental/10.1103/PhysRevB.105.224106> for description of optical methods, thermal processing details, and temperature dependent spectra of Er<sup>3+</sup>:MgO.
- [27] G. Liu and B. Jacquier, *Springer Series in Materials Science* (Springer, New York, 2005).
- [28] C. M. Dodson and R. Zia, *Phys. Rev. B* **86**, 125102 (2012).
- [29] R. Stephens and I. Malitson, *J. Res. Natl. Bur. Stand.* **49**, 249 (1952).
- [30] K. Lea, M. Leask, and W. Wolf, *J. Phys. Chem. Solids* **23**, 1381 (1962).
- [31] C. White, C. McHargue, P. Sklad, L. Boatner, and G. Farlow, *Mater. Sci. Rep.* **4**, 41 (1989).
- [32] Z. J. Kiss, *J. Chem. Phys.* **38**, 1476 (1963).
- [33] R. A. Cowley, *Philos. Trans. R. Soc. London Ser. A* **354**, 2799 (1996).
- [34] R. A. Evarestov, E. Blokhin, D. Gryaznov, E. A. Kotomin, and J. Maier, *Phys. Rev. B* **83**, 134108 (2011).
- [35] W. L. Bond, *J. Appl. Phys.* **36**, 1674 (1965).
- [36] S. Singh, J. P. Remeika, and J. R. Potopowicz, *Appl. Phys. Lett.* **20**, 135 (1972).
- [37] T. D. Dunbar, W. L. Warren, B. A. Tuttle, C. A. Randall, and Y. Tsur, *J. Phys. Chem. B* **108**, 908 (2004).
- [38] M. Debenham, *Appl. Opt.* **23**, 2238 (1984).
- [39] C. Yu and F. Bryant, *J. Lumin.* **18-19**, 841 (1979).
- [40] B. G. Enrique, *J. Chem. Phys.* **55**, 2538 (1971).
- [41] G. Wolfowicz, F. J. Heremans, and D. D. Awschalom, *Opt. Lett.* **46**, 4852 (2021).
- [42] S. Baccaro, L. Barone, B. Borgia, F. Castelli, F. Cavallari, I. Dafinei, F. de Notaristefani, M. Diemoz, A. Festinesi, E. Leonardi, E. Longo, M. Montecchi, and G. Organtini, *Nucl. Instrum. Methods Phys. Res. Sect. A* **385**, 209 (1997).
- [43] F. Cornacchia, A. Toncelli, M. Tonelli, E. Favilla, K. A. Subbotin, V. A. Smirnov, D. A. Lis, and E. V. Zharikov, *J. Appl. Phys.* **101**, 123113 (2007).
- [44] S. Bertain (private communication).
- [45] S. Welinski, A. Tiranov, M. Businger, A. Ferrier, M. Afzelius, and P. Goldner, *Phys. Rev. X* **10**, 031060 (2020).
- [46] L. Lajaunie, F. Boucher, R. Dessapt, and P. Moreau, *Phys. Rev. B* **88**, 115141 (2013).
- [47] V. K. Sabhapathi, O. M. Hussain, S. Uthanna, B. S. Naidu, and P. J. Reddy, *J. Mater. Sci. Lett.* **14**, 411 (1995).
- [48] M. Vila, C. Díaz-Guerra, D. Jerez, K. Lorenz, J. Piqueras, and E. Alves, *J. Phys. D* **47**, 355105 (2014).
- [49] P. Udvarhelyi, R. Nagy, F. Kaiser, S. Y. Lee, J. Wrachtrup, and A. Gali, *Phys. Rev. Appl.* **11**, 044022 (2019).
- [50] E. Alves, E. Rita, U. Wahl, J. G. Correia, T. Monteiro, J. Soares, and C. Boemare, in *Nuclear Instruments and Methods in Physics Research, Section B: Beam Interactions with Materials and Atoms* (North-Holland, Amsterdam, 2003), Vol. 206, pp. 1047–1051.

- [51] E. Alves, M. da Silva, J. Soares, R. Vianden, J. Bartels, and A. Kozanecki, *Nucl. Instrum. Methods Phys. Res. Sect. B* **147**, 383 (1999).
- [52] H. Przybylinska, W. Jantsch, Y. Suprun-Belevitch, M. Stepikhova, L. Palmetshofer, G. Hendorfer, A. Kozanecki, R. J. Wilson, and B. J. Sealy, *Phys. Rev. B* **54**, 2532 (1996).
- [53] A. Gritsch, L. Weiss, J. Früh, S. Rinner, and A. Reiserer, [arXiv:2108.05120](https://arxiv.org/abs/2108.05120).
- [54] R. E. George, J. P. Edwards, and A. Ardavan, *Phys. Rev. Lett.* **110**, 027601 (2013).
- [55] J. Liu, V. V. Laguta, K. Inzani, W. Huang, S. Das, R. Chatterjee, E. Sheridan, S. M. Griffin, A. Ardavan, and R. Ramesh, *Sci. Adv.* **7**, eabf8103 (2021).
- [56] D. M. Lukin, A. D. White, R. Trivedi, M. A. Guidry, N. Morioka, C. Babin, Ö. O. Soykal, J. Ul-Hassan, N. T. Son, T. Ohshima, P. K. Vasireddy, M. H. Nasr, S. Sun, J.-P. W. MacLean, C. Dory, E. A. Nanni, J. Wrachtrup, F. Kaiser, and J. Vučković, *npj Quantum Inf.* **6**, 80 (2020).
- [57] C. Thiel, T. Böttger, and R. Cone, *J. Lumin.* **131**, 353 (2011).
- [58] G. Wolfowicz, F. J. Heremans, C. P. Anderson, S. Kanai, H. Seo, A. Gali, G. Galli, and D. D. Awschalom, *Nat. Rev. Mater.* **6**, 906 (2021).
- [59] M. J. Graham, J. M. Zadrozny, M. S. Fataftah, and D. E. Freedman, *Chem. Mater.* **29**, 1885 (2017).